

Article

Not peer-reviewed version

Operando NRVS on LiFePO₄ Battery with ⁵⁷Fe Phonon DOS

[Alexey Rulev](#)*, Nobumoto Nagasawa, Haobo Li, [Hongxin Wang](#), [Stephen P. Cramer](#), Qianli Chen, Yoshitaka Yoda, [Artur Braun](#)*

Posted Date: 11 September 2025

doi: 10.20944/preprints202509.1009.v1

Keywords: NRVS; vibrational spectroscopy; phonon DOS; LiFePO₄; lithium ion battery



Preprints.org is a free multidisciplinary platform providing preprint service that is dedicated to making early versions of research outputs permanently available and citable. Preprints posted at Preprints.org appear in Web of Science, Crossref, Google Scholar, Scilit, Europe PMC.

Copyright: This open access article is published under a Creative Commons CC BY 4.0 license, which permit the free download, distribution, and reuse, provided that the author and preprint are cited in any reuse.

Disclaimer/Publisher's Note: The statements, opinions, and data contained in all publications are solely those of the individual author(s) and contributor(s) and not of MDPI and/or the editor(s). MDPI and/or the editor(s) disclaim responsibility for any injury to people or property resulting from any ideas, methods, instructions, or products referred to in the content.

Article

Operando NRVS on LiFePO₄ Battery with ⁵⁷Fe Phonon DOS

Alexey Rulev ^{1,*}, Nobumoto Nagasawa ², Haobo Li ³, Hongxin Wang ⁴, Stephen P. Cramer ⁴, Qianli Chen ³, Yoshitaka Yoda ² and Artur Braun ^{1,*}

¹ Laboratory for High Performance Ceramics, Empa. Swiss Federal Laboratories for Materials Science and Technology, Überlandstrasse 129, CH - 8600 Dübendorf, Switzerland

² SETI Institute, Mountain View, CA 94043, USA

³ Global College, Shanghai Jiao Tong University, Shanghai, 200240, China

⁴ Precision Spectroscopy Division, SPring-8/ JASRI, Sayo, Hyogo 679-5198, Japan

* Correspondence: artur.braun@alumni.ethz.ch

Abstract

The vibration properties of materials play a role in their conduction of electric charges. Relevant in this respect are also ionic conductors such as electrodes and solid electrolytes. The vibration properties are typically assessed with infrared and Raman spectroscopy, and inelastic neutron scattering, which all allow for the derivation of the phonon density of states (PDOS) in part of full portion of the Brillouin zone. A novel method is nuclear resonant vibration spectroscopy (NRVS), which produces the element specific PDOS from Mössbauer active isotopes in a compound. We have employed NRVS *operando* on a pouch cell battery containing a Li⁵⁷FePO₄ electrode and thus could derive the PDOS of the ⁵⁷Fe in the electrode during charging and discharging. The spectra reveal reversible vibrational changes associated with the two-phase conversion between LiFePO₄ and FePO₄, as well as signatures of metastable intermediate states. We demonstrate how the NRVS data can be used to tune the atomistic simulations to accurately reconstruct the full vibration structures of the battery materials in *operando* conditions. Unlike optical techniques, NRVS provides bulk-sensitive, element-specific access to the full phonon spectrum under realistic *operando* conditions. These results establish NRVS as a powerful method to probe lattice dynamics in working batteries and to advance the understanding of ion transport and phase transformation mechanisms in electrode materials.

Keywords: NRVS; vibrational spectroscopy; phonon DOS; LiFePO₄; lithium ion battery

1. Introduction

Lithium iron phosphate (LFP) with olivine structure is one of the main cathode materials for lithium-ion batteries. One of the main advantages that make the olivine cathode an attractive material is the improved stability compared to the layered cathodes like nickel-manganese-cobalt oxides [1]. One of the drawbacks of olivine cathodes is the slower cycling rate, which is limited mostly by solid-state diffusion within the olivine structure. Lithium diffuses through 1-D channels framework in olivine structure, which is generally considered slower than 2-D diffusion in layered oxides.

The ionic diffusion in solids, especially in case of light ions, is a complex process where many parameters are involved. For example, it was proposed that some vibration modes of the lattice may propel the ionic transport by dynamically lowering the jump barrier. It was shown that low-energy phonons in olivine structure enhance lithium diffusion, allowing the higher cycling rate [2]. Generally, the lower phonon frequencies suggest softer lattice and enhanced ionic transport, so phonon density of states can be used as a predictor for ionic conductivity [3,4]. Therefore, understanding the vibration properties of the cathode material is crucial for understanding the solid-state mass transfer phenomena and for designing the materials for fast charging devices.

Study of vibration properties of battery materials, especially in *operando* conditions, is a complex task. The most convenient techniques like optical (Raman or IR) vibrational spectroscopy lack penetration depth, so they require notable modifications of the cell and material to make acquisition of the signal possible. Such modifications like holes in current collector or separator often lead to non-uniform current distribution and distorted signal [5]. Moreover, the carbon coating, that is common in LFP cathodes, was shown to block the Raman and IR signal from iron phosphate [6]. In addition, the information obtained from IR or Raman spectra gives only limited insights of the phonon structure, as it only shows some modes around gamma-point of Brillouin zone. Techniques like inelastic neutron scattering can be used to study the vibrational properties of active materials. It was demonstrated that the difference between surface and bulk phonons, measured with INS, allows us to get some insights on morphology of the active particles. Despite the great penetration depth of neutrons, the technique is not very well suited for *operando* conditions due to many components of the battery that obfuscate already complex signal.

Thanks to the presence of iron in the structure, LFP opens the possibility to use techniques based on nuclear resonance, like Mössbauer spectroscopy. Such techniques suit perfectly for *operando* experiments due to combination of signal penetration depth and element specificity, that guarantees that signal is coming exclusively from the cathode material. The nuclear resonance vibrational spectroscopy (NRVS) is a synchrotron-based technique that allows to study the vibrational density of states, projected on a Mössbauer-active element [7]. This technique was used to study the dynamics of active centers in biological systems [8], or the phonon structure of crystalline solids [9]. Here we for the first time demonstrate the *operando* study of the phonon structure of an active cathode material using NRVS technique during the cell cycling.

2. Materials and Methods

2.1. Synthesis

^{57}Fe -enriched LFP was synthesized using the modified method from [10]. We need to mention here that ^{57}Fe isotope is hardly available as salt or oxide. We were therefore required to develop our own synthesis route, illustrated in the flow diagram in Figure 1, based with available iron metal. As a source of ^{57}Fe isotope, ^{57}Fe -enriched metal foil (Neonest AB (BuyIsotope.com), SE-171 50 Solna, Sweden) was used, the isotope contents of which detailed in Table 1 and according to which the ^{57}Fe content is larger than 96%.

Table 1. Atomic % concentration of the Fe isotopes of the nominal ^{57}Fe iron sample as provided by the Certificate of Analysis № 240801- 089Sct by Neonest AB issued on 1. September 2025.

Isotope:	Fe-54	Fe-56	Fe-57	Fe-58
Content (at. %):	0.005	0.615	96.060	3.360

3.5 ml of concentrated HNO_3 were mixed with 2 ml of deionized water and 0.5g of ^{57}Fe were dissolved in the nitric acid. After the complete dissolution, water was added to a total of ~9 ml of solution. Separately 0.63 g of P_2O_5 (Sigma-Aldrich) were slowly dissolved in 10 ml of water to obtain the H_3PO_4 solution. Then the H_3PO_4 solution was added dropwise to the iron nitride solution under intensive stirring. Then 5M NH_4OH solution was added to the mixture under stirring and heating at 50°C until pH reached value of ~4, when thick gel-like sediment was formed. The mixture was left stirring for at least 12 hours, then filtered on Buchner vacuum funnel and washed with deionized water until neutral pH. Then the sediment was dried at 60°C , ground in a mortar and dried again at 120°C for 5 hours. This resulted in an amorphous $\text{FePO}_4 \cdot x\text{H}_2\text{O}$ that does not show any Bragg reflections. A portion of amorphous $\text{FePO}_4 \cdot x\text{H}_2\text{O}$ was annealed at 650°C for 1 hour to estimate the amount of water and measure Raman spectra of delithiated FP. After annealing the amorphous FP crystallizes and the sample demonstrates narrow XRD peaks, corresponding to the FePO_4 crystal-line

phase. The mass loss after annealing was 11% so the estimated amount of water in amorphous powder was $x=1$.

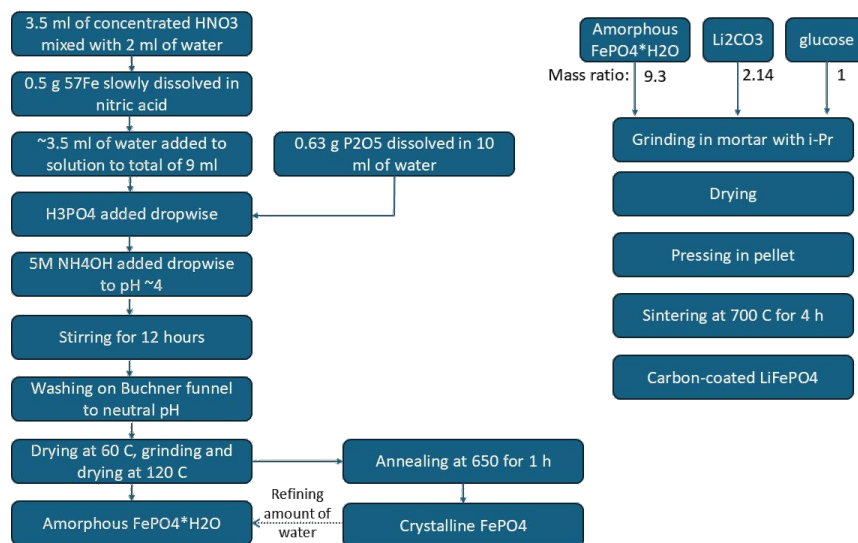


Figure 1. Flow diagram for our synthesis of iron phosphate and lithium iron phosphate with ^{57}Fe isotope metal sheet as raw material.

Stoichiometric amounts of amorphous $\text{FePO}_4 \cdot \text{H}_2\text{O}$ and Li_2CO_3 (5% excess) with 8 wt.% of total mixture mass of glucose (final mass ratio: $\text{FePO}_4 \cdot \text{H}_2\text{O} : \text{Li}_2\text{CO}_3 : \text{glucose} = 9.3 : 2.14 : 1$) were mixed in a mortar with isopropanol and thoroughly ground, then dried at 60°C for 1 hour. Then the mixture was pressed in a pellet and sintered at 700°C for 4 hours resulting in black pellet. The sintered pellet was then crushed and ground in a mortar, resulting in LiFePO_4 particles covered with carbon. The phase composition was validated with XRD, demonstrating LFP phase with small amount of impurities.

2.2. Pouch Cell Battery Assembly

The obtained powder was assembled to a battery positive electrode as follows. To prepare the slurries, LFP powder was mixed with polyvinylidene fluoride dissolved in N-Methyl-2-pyrrolidone (NMP) and carbon black (super C-65) in mass ratio 90:5:5 and mixed in a planetary mixer. The slurries were cast on Al foil with a doctor blade applicator, dried at 80°C in air, then pressed and vacuum-dried in the antechamber of the glovebox. The resulting active material mass loading was approximately 8 mg/cm².

The cells were assembled in a glove box in argon (Ar) atmosphere. As a counter electrode graphite on Cu foil was used (active material loading ~12 mg/cm²). The electrodes were separated with Whatman glass-fiber separator, and approximately 800 μl of 1M LiPF_6 solution in a mixture of ethylene carbonate : diethyl carbonate : dimethyl carbonate (1:1:1 mass) were added as electrolyte. Cells were assembled in a pouch case with a 7×14 mm window covered with Kapton tape. During the experiment the cell was clamped with an aluminum frame to ensure tight contact between the electrodes. The photo of the cell and the placement of the cell in the beamline are displayed in Figure 2.



Figure 2. (left) Photo of the *operando* cell with Kapton window. (right) photo of the cell in the endstation of the beamline BL19LXU at SPring-8.

2.3. Battery Charging and Discharging

The cell was cycled with IVIUM Vertex.100mA potentiostat at constant current at the rate of approx. C/30 (50 $\mu\text{A}/\text{cm}^2$). After reaching the threshold potential of 4.2 V, the cell was held potentiostatically for ~ 1 hour at this potential and then discharged at the same rate.

2.4. Nuclear Resonant Vibration Spectroscopy

Nuclear resonance vibration spectroscopy was performed at beamline BL19LXU at Spring-8 in Hyogo, Japan [11,12]. The incident X-ray energy was set around 14.413 keV to excite the γ -transition of ^{57}Fe [13]. The spectra were acquired in the range from approximately -42 to +65 meV from the elastic peak. Spectra were acquired continuously in *operando* mode, with each spectrum acquisition taking approximately 20 minutes. This means that the state of charge of the battery was not kept constant while the NRVS scans were in course. NRVS spectra were processed using "NRVS tool" from spectra.tools [14] PHOENIX software [15] to obtain the Fe-projected phonon density of states (PDOS).

We briefly explain how an NRVS spectrum is generated [7,14]. The battery cell containing ^{57}Fe is scanned (this is not a scan over position, but a scan of the energy) with the X-ray beam energy in the aforementioned range covering the nuclear γ -transition at $E_1 = 14.413$ keV of ^{57}Fe with included vibrational levels. This results in nuclear back radiation of scattered energy $E_2 = h\nu_1$, comparable to the scheme on the left of Figure 1 in our previous publication [9]. There is also X-ray fluorescence from the K shell electrons of ^{57}Fe by internal conversion with energy $h\nu_2$. The X-ray intensities at $h\nu_1$ and $h\nu_2$ are recorded versus the vibration energy $E_{\text{vib}} = E_1 - E_2 = 14.413$ keV - $h\nu_1$. The resulting spectrum is comparable with an optical Raman spectrum with elastic peak and Stokes and anti-Stokes shifted peaks. But it probes only the ^{57}Fe .

2.5. Optical Raman Spectroscopy

Optical Raman spectra of the carbon-coated LFP powder, the LFP powder cast on Al foil and annealed FP powder were obtained using a Renishaw inVia Qontor spectrometer. The laser wavelength was 532 nm, with 10 s exposure time, 6% power (1.9 mW) and 5 accumulations. A representative spectrum is shown in Figure 8. For comparison, the Raman shifts of LFP and FP agree well with the characteristic peaks documented and explained in the publications by Wu et al. [16] and Zhang et al. [17], respectively.

2.6. Calculation of Total and Partial Vibrational Density of States (PVDOS)

Phonon properties were simulated using a deep-learning atomistic model MatterSim [18]. To obtain the Fe-projected phonon density of states (PDOS), the structures were relaxed, and the phonon structure was calculated using finite displacement method using PHONOPY code [19,20] with applied non-analytical term correction (NAC). The dielectric constant and Born effective charges for the NAC were calculated using Quantum ESPRESSO package [21–23]. To compare with the experimental phonon DOS, the gaussian broadening was applied to the calculated phonon DOS with the width derived from the elastic peak in the experimental spectra, which was taken as a resolution function.

3. Results and Discussion

3.1. Crystallographic Structure

The X-ray diffractograms of the pristine LFP material show in Figure 3 that the samples are phase-pure LFP.

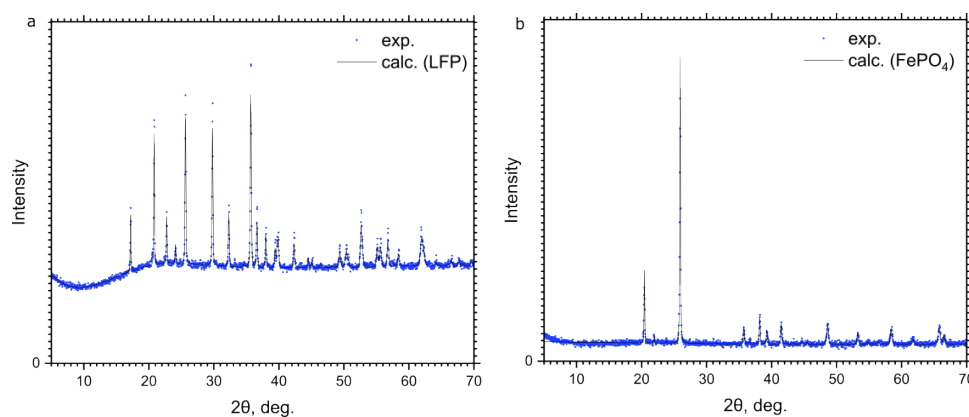


Figure 3. (a) X-ray diffractograms of LFP and (b) FP. Shown are the measured data points and the profile from Rietveld refinement.

Rietveld refinement shows a slight, ~10% deficiency in lithium positions, which may be associated with lithium sublimation during the annealing [24] despite the excess of lithium carbonate. It is therefore plausible that the cells demonstrate a slightly lower total capacity (~135 mAh/g) is slightly lower than the usually observed values. The occupancy of all sites was determined by Rietveld refinement and is listed in Table 2.

Table 2. Occupancy parameters, obtained by Rietveld refinement of XRD of LFP. Occupancy of Fe was fixed to 1.

Atom	Fraction
Fe	1
Li	0.93(13)
P	1.025(30)
O1	0.84(7)
O2	0.86(6)
O3	0.88(6)

Figure 4, a shows the electrochemical cycling curve (voltage profile) of the cell, the corresponding NRVS *operando* spectra and the derived Fe-projected partial vibrational DOS (PVDOS). The cycling curve shows a slight slope in the beginning of charging and a sharp voltage drop on discharge before the end of charge. We speculate that this observation might come from

moisture from the outside, which may have leaked into the cell through the Kapton window, which is known to be permeable for water [25–28]. Nevertheless, the NRVS spectra show the reversible behavior with the changes still happening after the voltage drop at ~35 hours. This indicates that the lithiation of LFP continues, which can be explained by extraction of lithium from the electrolyte due to water-related loss of lithium inventory.

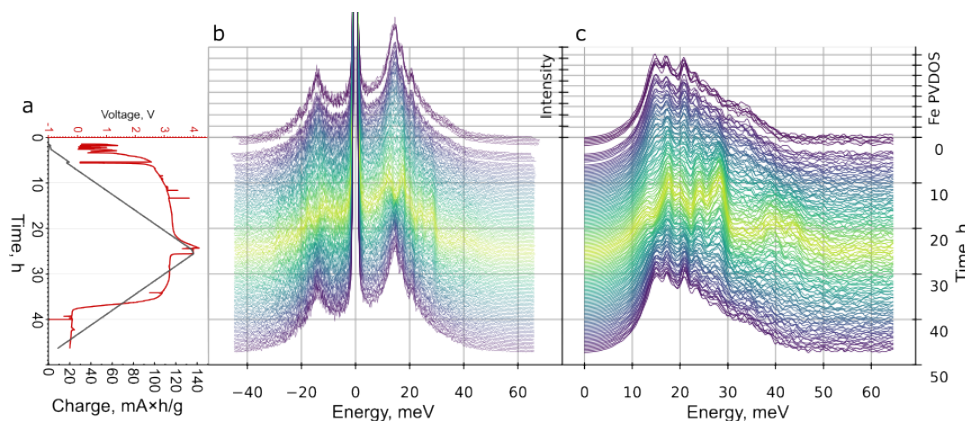


Figure 4. (a) Voltage profile of the cell during *operando* experiment and the total charge passed through the cell. (b) raw NRVS spectra, collected from the cell. The spectra were centered so that the energy of the elastic peak is zero. (c) Fe-projected partial vibrational density of states, derived from the NRVS spectra.

The NRVS spectra show reversible changes upon lithiation and delithiation, which correspond to the two-phase conversion:



Figure 4, c displays the Fe-projected PVDOS, obtained from the NRVS spectra. The phonon DOS clearly demonstrates the decrease of the peaks at ~15 and 20 meV and appearance of peaks at ~29 and 35–45 meV upon delithiation. We used the PVDOS in the initial state and the PVDOS obtained at the end of charging as the basis components and fitted all the intermediate PVDOS with a linear combination of the two basis components. The coefficients as a function of time and charge are shown in Figure 5. The linear relation between charge and the fraction of components indicates that all the intermediate spectra are at large composed of two phases that represent fully lithiated and delithiated states, which are LiFePO_4 and FePO_4 . Figure 5, d shows the residuals of the least square fit, obtained by equation:

$$R_i = S_i - (a_1 \cdot S_{init} + a_2 \cdot S_f)$$

where S_i , S_{init} and S_f are i -th PVDOS, initial PVDOS in fully lithiated state, and the final PVDOS in the fully charged state, respectively, a_1 and a_2 are the coefficients shown in Figure 5, a and b. The residuals show a systematic pattern for intermediate states (Figure 5, d). The pattern looks symmetrical for the charge and discharge half-cycles, what indicates that it does not originate from the change of the state during the spectrum acquisition but is an indicator of presence of more phases [18] than just FP and LFP. It was previously reported that the conversion from LFP to FP goes via the metastable intermediate phase [29,30], which was detected with NRVS. At a certain state of charge the notable change of the pattern can be observed: for example, the peak at ~16 meV disappears, and the peak at 20 meV appears. We cannot rule out, based on the observed reversible change of the pattern, more than one intermediate phase. Confirmation of such scenario would require further study.

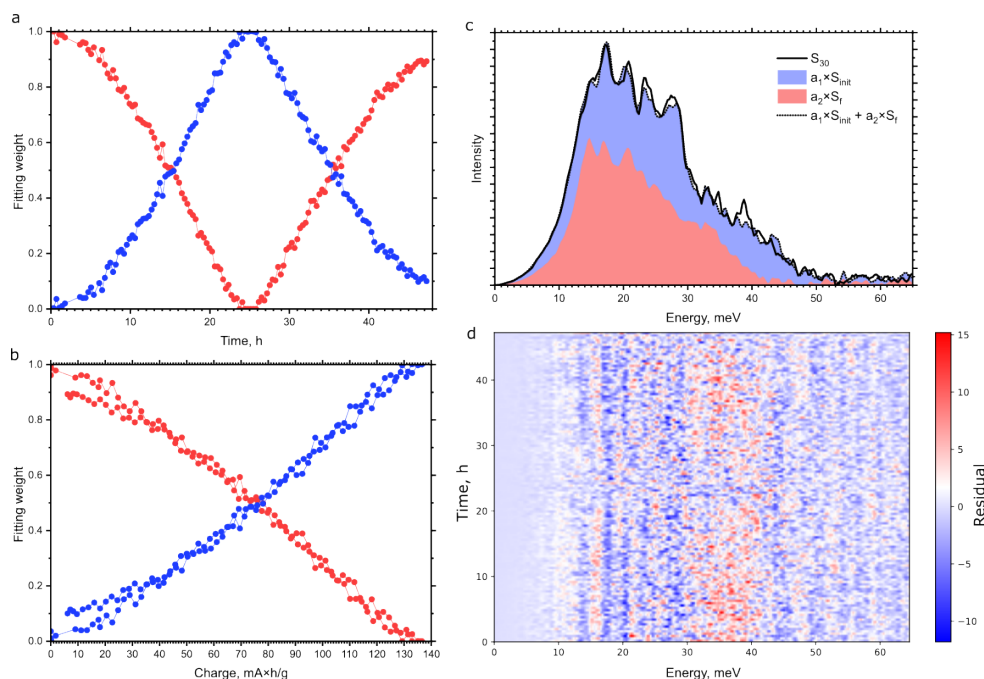


Figure 5. Weights a_1 and a_2 of fitting all experimental DOS versus time (a) and charge (b). (c) Example of fitting an intermediate PVDOS (S_{30}) with a linear combination of initial and final PVDOS. (d) Residuals of the fitting of all spectra as a function of time of measurement from the start of experiment.

Figure 6 displays the comparison between the experimental Fe PVDOS in fully charged and fully discharged states and calculated PVDOS of FP and LFP. While for the FP phase the perfect agreement between the experimental and calculated data was achieved immediately, for the LFP the best fit was achieved by stretching the energy scale of calculated data by a factor of 1.064. Application of such scaling is usual for the simulated vibrational spectra [31] and is justified by the semi-empirical nature of DFT (the choice of exchange-correlation functional and Hubbard U parameters). This way, NRVS here was used to tune the model to the experimental data. Such tuning is additionally verified by the good fitting of the experimental Raman spectrum, as shown in Figure 5. For example, the highest peak at ~ 118 meV, which corresponds to the vibrations of PO_4 tetrahedra and is not directly related to Fe atoms, is also precisely reproduced by the simulation, fitted to experimental NRVS.

Our experimental PVDOS lends empirical confirmation to our calculations and support also those DFT calculations, which are reported in the literature [32]. The MatterSim [18] force field was shown to simulate the phonon properties with level of accuracy close to that of DFT [33], giving confidence in the simulation results. This way, the NRVS data can serve to tune the calculation parameters and validate the calculated vibration structure.

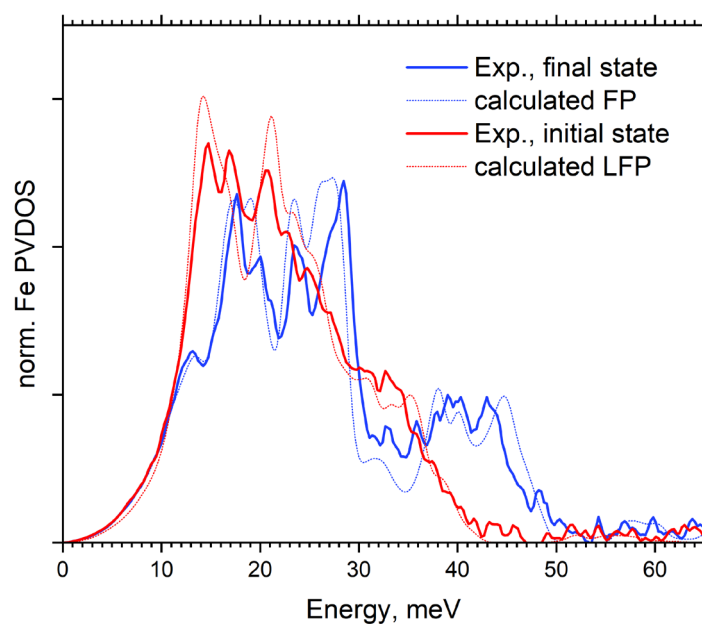


Figure 6. Experimental (solid lines) and calculated (dotted lines) PVDOS of Fe in LFP and FP.

The calculated PVDOS of FP reproduces the experimental one with great accuracy, reproducing all the observed features. The PVDOS of LFP, however, shows slight deviation between the experiment and calculations, with a peak at ~ 17 meV not reproduced by calculations. This may be attributed to the presence of Li vacancies in the initial state, which is not fully lithiated, which may introduce additional features to the phonon structure. The same phenomenon led to the systematic error, shown in Figure 3, d, which is presumably produced by the presence of the third intermediate phase, which may have some ordered Li vacancies, and whose phonon spectrum cannot be described as a linear combination of the fully lithiated and fully delithiated phases.

Figure 5 shows the experimental optical Raman spectrum of LFP and the NRVS-derived PVDOS in comparison with the calculated phonon structure. The Raman spectrum agrees with the reported in literature *in situ* [16,34] or *ex situ* [17] spectra. For the orientation of the reader: the prominent peak at below 120 meV corresponds to the symmetric stretch vibration of the phosphate cage PO_3^{4-} with $\nu_1 \approx 950$ eV. Due to the experimental constraints, the *in situ* Raman spectra reported in the literature only allows to observe the highest peak at ~ 950 cm^{-1} ($= 118$ meV) that corresponds to the relatively flat band, associated with PO_4 tetrahedra vibrations with A_g symmetry. The two smaller peaks at 123 meV and 132 meV are the asymmetric stretch of the same structure. The vibrations of PO_4 octahedra obviously are sensitive to the presence of lithium in the crystal structure, allowing to monitor the lithium content in the material.

The vibrations associated with Fe all have lower energy and are confined below ~ 50 meV (≈ 400 cm^{-1} , this is around the two well developed peaks at 22 and 35 meV, corresponding to 220 and 290 cm^{-1} with translation or Fe and coupled translation and vibration of the phosphate cage), so the *operando* NRVS focuses on the different regions of the vibration structure. Wu et al. find this region interesting because of the prominent differences between lithiated and non-lithiated material [16]. It was shown that vibrations in this region may indicate differences in microstructure [32]; in addition, our results show that they also allow to monitor the lithium content, and to study the superstructure, formed in the intermediate phase, as shown above.

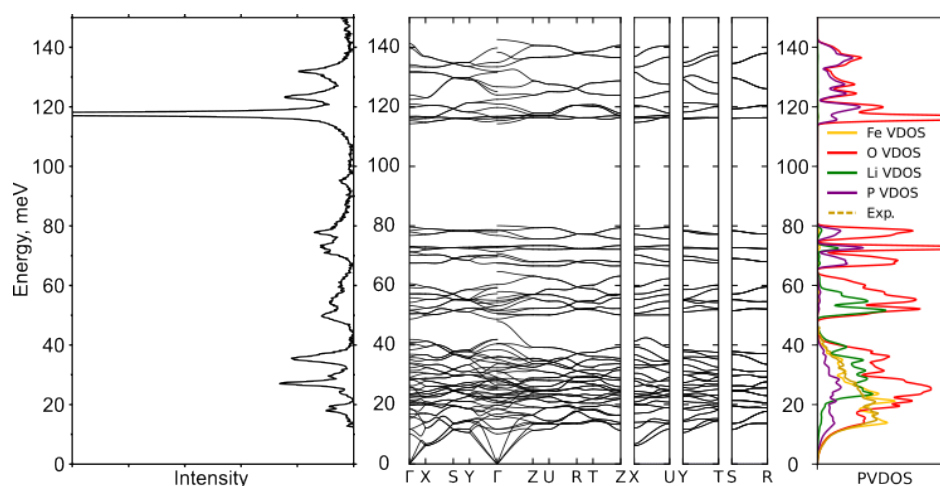


Figure 7. left: Raman spectrum of LFP powder; center: calculated phonon band structure; right: calculated element-projected PVDOS and NRVS-derived experimental Fe PVDOS.

While the Fe vibrations are not directly affected by the presence of lithium, they have strong overlap with the vibrations of oxygen and phosphorus, as shown in Figure 7. Upon delithiation the vibrations of Fe shift to the higher energies (Figure 3) same way as the Raman peaks [16,34] due to lattice contraction and stiffening of Fe-O bonds.

Compared to the other vibrational spectroscopy techniques, NRVS gives valuable insights into the phonon structure of the material. It allows to perform *operando* measurements with high temporal resolution. The acquisition of a single spectrum in our experiments took approx. 20 minutes, providing decent statistics to reconstruct the PVDOS with sufficient accuracy. It also does not require substantially large amounts of material and provides the component specificity (i.e., it focuses on the signal from the active material), in contrast, for example, to the inelastic neutron scattering. In addition, it provides higher energy resolution, than usually available for inelastic neutron scattering [35]. Another significant advantage is that it allows for measuring the realistic cell with minimal modifications to allow the *operando* measurement thanks to high penetration depth of high-energy X-rays.

Conclusions

We have described the experiment to measure the vibrational properties of the active electrode material of Li-ion battery with NRVS technique. We have demonstrated that this technique is a powerful tool and is very well suited for *operando* setup, compared to other vibrational spectroscopy techniques.

It was previously shown that vibrational spectroscopy allows to detect phenomena associated with the microstructure of the material. By combining the prior structural knowledge with the experimental vibrational data, computational simulations allow us to precisely reconstruct the vibrational structure, which allows not only to derive the various thermodynamical properties, but also to get insights into the atomic structure or microstructure of the material.

Author Contributions: Conceptualization, A.B. and A.R.; methodology, A.B., S.P.C., and H.W; validation, A.R., Y.Y., A.B, Q.C.; formal analysis, A.R., A.B., H.L.; investigation, A.B. and A.R.; resources, N.H., Y.Y., Q.C. H.L.; writing—original draft preparation, A.R., A.B; writing—review and editing, A.R. A.B.; visualization, A.R., H.L.; supervision, A.B.; project administration, A.B.; funding acquisition, A.B. All authors have read and agreed to the published version of the manuscript.

Funding: This work was funded by the European Commission Green Deal program as Euramet metrology projects 21GRD01 and 24GRD09 via Swiss State Secretariat of Education and Research Übergangsmassnahmen Horizon-Paket 2021-2027 Kredit A231.0435, Contract number 22.00459. S.P.C. acknowledges financial support by project US NIH GM65440. The NRVS synchrotron radiation experiments were performed at BL19LXU of

SPring-8 with the approval of the Japan Synchrotron Radiation Research Institute (JASRI) (Proposal No 2024B1461). NRVS raw data treatment was performed under the XSIM project on the CORI computing system at NERSC, a U.S. Department of Energy Office of Science User Facility operated under Contract No. DE-AC02-05CH11231. We are grateful to Georg Spescha for information on water permeability on polyimide, and Corsin Battaglia and Edouard Querel (all Empa) for providing the hardware for electrode coating hardware and cell assembly.

Data Availability Statement: The data can be obtained upon personal request by contacting Artur Braun and Alexey Rulev.

Acknowledgments: We are grateful to Leland B. Gee (SSRL SLAC, Stanford) for support with the conversion software for NRVS raw spectra

Conflicts of Interest: The authors declare no conflicts of interest.

Abbreviations

The following abbreviations are used in this manuscript:

PDOS	Phonon Density of States
NRVS	Nuclear Resonant Vibration Spectroscopy
LFP	Lithium Iron Phosphate
IR	Infra-Red
FP	Iron Phosphate
XRD	X-ray Diffraction
NMP	N-Methyl-2-pyrrolidone
DOS	Density of States
PVDOS	Partial Vibrational Density of States
NAC	non-analytical term correction

References

1. Evro, S.; Ajumobi, A.; Mayon, D.; Tomomewo, O.S. Navigating battery choices: A comparative study of lithium iron phosphate and nickel manganese cobalt battery technologies. *Future Batteries* **2024**, *4*. <https://doi.org/10.1016/j.fub.2024.100007>.
2. Oh, H.; Noh, C.; Cho, A.Y.; Kim, J.C.; Kim, N.; Kim, K.H. Enhancing 1D ionic conductivity in lithium manganese iron phosphate with low-energy optical phonons. *Sci Rep* **2025**, *15*, 28421. <https://doi.org/10.1038/s41598-025-13769-8>.
3. Sagotra, A.K.; Chu, D.; Cazorla, C. Influence of lattice dynamics on lithium-ion conductivity: A first-principles study. *Physical Review Materials* **2019**, *3*. <https://doi.org/10.1103/PhysRevMaterials.3.035405>.
4. Muy, S.; Schlem, R.; Shao-Horn, Y.; Zeier, W.G. Phonon-Ion Interactions: Designing Ion Mobility Based on Lattice Dynamics. *Advanced Energy Materials* **2020**, *11*. <https://doi.org/10.1002/aenm.202002787>.
5. Rosser, T.E.; Dickinson, E.J.F.; Raccichini, R.; Hunter, K.; Searle, A.D.; Kavanagh, C.M.; Curran, P.J.; Hinds, G.; Park, J.; Wain, A.J. Improved Operando Raman Cell Configuration for Commercially-Sourced Electrodes in Alkali-Ion Batteries. *Journal of The Electrochemical Society* **2021**, *168*. <https://doi.org/10.1149/1945-7111/ac132d>.
6. Zaghbi, K.; Mauger, A.; Goodenough, J.B.; Julien, C.M. Design and Properties of LiFePO₄ Nano-materials for High-Power Applications. In *Nanotechnology for Lithium-Ion Batteries*; Nanostructure Science and Technology; 2012; pp. 179-220.
7. Wang, H.; Braun, A.; Cramer, S.P.; Gee, L.B.; Yoda, Y. Nuclear Resonance Vibrational Spectroscopy: A Modern Tool to Pinpoint Site-Specific Cooperative Processes. *Catalysts* **2021**, *11*. <https://doi.org/10.3390/cryst11080909>.

8. Xiao, Y.M.; Fisher, K.; Smith, M.C.; Newton, W.E.; Case, D.A.; George, S.J.; Wang, H.X.; Sturhahn, W.; Alp, E.E.; Zhao, J.Y.; et al. How nitrogenase shakes - Initial information about P-cluster and FeMo-cofactor normal modes from nuclear resonance vibrational Spectroscopy (NRVS). *Journal of the American Chemical Society* **2006**, *128*, 7608-7612. <https://doi.org/10.1021/ja0603655>.
9. Rulev, A.; Wang, H.; Erat, S.; Aycibin, M.; Rentsch, D.; Pomjakushin, V.; Cramer, S.P.; Chen, Q.; Nagasawa, N.; Yoda, Y.; et al. 119Sn Element-Specific Phonon Density of States of BaSnO₃. *Crystals* **2025**, *15*. <https://doi.org/10.3390/cryst15050440>.
10. Zhu, Y.; Tang, S.; Shi, H.; Hu, H. Synthesis of FePO₄·xH₂O for fabricating submicrometer structured LiFePO₄/C by a co-precipitation method. *Ceramics International* **2014**, *40*, 2685-2690. <https://doi.org/10.1016/j.ceramint.2013.10.055>.
11. Baron, A.Q.R.; Tanaka, Y.; Miwa, D.; Ishikawa, D.; Mochizuki, T.; Takeshita, K.; Goto, S.; Matsushita, T.; Kimura, H.; Yamamoto, F.; et al. Early commissioning of the SPring-8 beamline for high resolution inelastic X-ray scattering. *Nuclear Instruments and Methods in Physics Research Section A: Accelerators, Spectrometers, Detectors and Associated Equipment* **2001**, *467-468*, 627-630. [https://doi.org/10.1016/s0168-9002\(01\)00431-4](https://doi.org/10.1016/s0168-9002(01)00431-4).
12. Yoda, Y. X-ray beam properties available at the nuclear resonant scattering beamline at SPring-8. *Hyperfine Interactions* **2019**, *240*. <https://doi.org/10.1007/s10751-019-1598-3>.
13. Sprouse, G.D.; Hanna, S.S. Gamma ray transitions in 57Fe. *Nuclear Physics* **1965**, *74*, 177-183. [https://doi.org/10.1016/0029-5582\(65\)90257-9](https://doi.org/10.1016/0029-5582(65)90257-9).
14. Gee, L.B.; Wang, H.; Cramer, S.P. NRVS for Fe in Biology: Experiment and Basic Interpretation. *Methods Enzymol.* **2018**, *599*, 409-425. <https://doi.org/10.1016/bs.mie.2017.11.002>.
15. Sturhahn, W. CONUSS and PHOENIX: Evaluation of nuclear resonant scattering data. *Hyperfine Interactions* **2000**, *125*, 149-172. <https://doi.org/10.1023/a:1012681503686>.
16. Wu, J.; Dathar, G.K.; Sun, C.; Theivanayagam, M.G.; Applestone, D.; Dylla, A.G.; Manthiram, A.; Henkelman, G.; Goodenough, J.B.; Stevenson, K.J. In situ Raman spectroscopy of LiFePO₄: size and morphology dependence during charge and self-discharge. *Nanotechnology* **2013**, *24*, 424009. <https://doi.org/10.1088/0957-4484/24/42/424009>.
17. Zhang, L.; Brow, R.K. A Raman Study of Iron-Phosphate Crystalline Compounds and Glasses. *Journal of the American Ceramic Society* **2011**, *94*, 3123-3130. <https://doi.org/10.1111/j.1551-2916.2011.04486.x>.
18. Yang, H.; Hu, C.; Zhou, Y.; Liu, X.; Shi, Y.; Li, J.; Li, G.; Chen, Z.; Chen, S.; Zeni, C.; et al. MatterSim: A Deep Learning Atomistic Model Across Elements, Temperatures and Pressures. **2024**, arXiv:2405.04967. <https://doi.org/10.48550/arXiv.2405.04967>.
19. Togo, A. First-principles Phonon Calculations with Phonopy and Phono3py. *Journal of the Physical Society of Japan* **2023**, *92*. <https://doi.org/10.7566/jpsj.92.012001>.
20. Togo, A.; Chaput, L.; Tadano, T.; Tanaka, I. Implementation strategies in phonopy and phono3py. *J Phys Condens Matter* **2023**, *35*. <https://doi.org/10.1088/1361-648X/acd831>.
21. Giannozzi, P.; Baroni, S.; Bonini, N.; Calandra, M.; Car, R.; Cavazzoni, C.; Ceresoli, D.; Chiarotti, G.L.; Cococcioni, M.; Dabo, I.; et al. QUANTUM ESPRESSO: a modular and open-source software project for quantum simulations of materials. *J Phys Condens Matter* **2009**, *21*, 395502. <https://doi.org/10.1088/0953-8984/21/39/395502>.
22. Giannozzi, P.; Andreussi, O.; Brumme, T.; Bunau, O.; Buongiorno Nardelli, M.; Calandra, M.; Car, R.; Cavazzoni, C.; Ceresoli, D.; Cococcioni, M.; et al. Advanced capabilities for materials modelling with Quantum ESPRESSO. *J Phys Condens Matter* **2017**, *29*, 465901. <https://doi.org/10.1088/1361-648X/aa8f79>.

23. Giannozzi, P.; Barone, O.; Bonfanti, P.; Brunato, D.; Car, R.; Carnimeo, I.; Cavazzoni, C.; de Gironcoli, S.; Delugas, P.; Ferrari Ruffino, F.; et al. Quantum ESPRESSO toward the exascale. *J Chem Phys* **2020**, *152*, 154105. <https://doi.org/10.1063/5.0005082>.
24. Halankar, K.K.; Mandal, B.P.; Jangid, M.K.; Mukhopadhyay, A.; Meena, S.S.; Acharya, R.; Tyagi, A.K. Optimization of lithium content in LiFePO₄ for superior electrochemical performance: the role of impurities. *RSC Adv* **2018**, *8*, 1140-1147. <https://doi.org/10.1039/c7ra10112k>.
25. Chen, G.Q.; Scholes, C.A.; Qiao, G.G.; Kentish, S.E. Water vapor permeation in polyimide membranes. *Journal of Membrane Science* **2011**, *379*, 479-487. <https://doi.org/10.1016/j.memsci.2011.06.023>.
26. GmbH, C.K. Water vapor permeability of various plastic films. Available online: <https://www.cmc.de/en/blog/know-how-5/water-vapor-permeability-of-various-plastic-films-181> (accessed on 12 August 2025).
27. Su, L.; Choi, P.; Parimalam, B.S.; Litster, S.; Reeja-Jayan, B. Designing reliable electrochemical cells for operando lithium-ion battery study. *MethodsX* **2021**, *8*, 101562. <https://doi.org/10.1016/j.mex.2021.101562>.
28. Bak, S.-M.; Shadik, Z.; Lin, R.; Yu, X.; Yang, X.-Q. In situ/operando synchrotron-based X-ray techniques for lithium-ion battery research. *NPG Asia Materials* **2018**, *10*, 563-580. <https://doi.org/10.1038/s41427-018-0056-z>.
29. Nishimura, S.; Natsui, R.; Yamada, A. Superstructure in the Metastable Intermediate-Phase Li_{2/3} FePO₄ Accelerating the Lithium Battery Cathode Reaction. *Angew Chem Int Ed Engl* **2015**, *54*, 8939-8942. <https://doi.org/10.1002/anie.201501165>.
30. Orikasa, Y.; Maeda, T.; Koyama, Y.; Murayama, H.; Fukuda, K.; Tanida, H.; Arai, H.; Matsubara, E.; Uchimoto, Y.; Ogumi, Z. Direct observation of a metastable crystal phase of Li(x)FePO₄ under electrochemical phase transition. *J Am Chem Soc* **2013**, *135*, 5497-5500. <https://doi.org/10.1021/ja312527x>.
31. Merrick, J.P.; Moran, D.; Radom, L. An evaluation of harmonic vibrational frequency scale factors. *J Phys Chem A* **2007**, *111*, 11683-11700. <https://doi.org/10.1021/jp073974n>.
32. Benedek, P.; Yazdani, N.; Chen, H.R.; Wenzler, N.; Juranyi, F.; Månsson, M.; Islam, M.S.; Wood, V.C. Surface phonons of lithium ion battery active materials. *Sustainable Energy & Fuels* **2019**, *3*, 508-513. <https://doi.org/10.1039/c8se00389k>.
33. Loew, A.; Sun, D.; Wang, H.-C.; Botti, S.; Marques, M.A.L. Universal machine learning interatomic potentials are ready for phonons. *npj Computational Materials* **2025**, *11*. <https://doi.org/10.1038/s41524-025-01650-1>.
34. Siddique, N.A.; Salehi, A.; Wei, Z.; Liu, D.; Sajjad, S.D.; Liu, F. Length-Scale-Dependent Phase Transformation of LiFePO₄: An In situ and Operando Study Using Micro-Raman Spectroscopy and XRD. *Chemphyschem* **2015**, *16*, 2383-2388. <https://doi.org/10.1002/cphc.201500299>.
35. Muy, S.; Bachman, J.C.; Giordano, L.; Chang, H.-H.; Abernathy, D.L.; Bansal, D.; Delaire, O.; Hori, S.; Kanno, R.; Maglia, F.; et al. Tuning mobility and stability of lithium ion conductors based on lattice dynamics. *Energy & Environmental Science* **2018**, *11*, 850-859. <https://doi.org/10.1039/c7ee03364h>.

Disclaimer/Publisher's Note: The statements, opinions and data contained in all publications are solely those of the individual author(s) and contributor(s) and not of MDPI and/or the editor(s). MDPI and/or the editor(s) disclaim responsibility for any injury to people or property resulting from any ideas, methods, instructions or products referred to in the content.